ACS APPLIED MATERIALS & INTERFACES

Research Article

www.acsami.org

Luffa-Sponge-Like Glass–TiO_2 Composite Fibers as Efficient Photocatalysts for Environmental Remediation

Zhijun Ma,[†] Weibo Chen,[‡] Zhongliang Hu,[‡] Xuanzhao Pan,[‡] Mingying Peng,[†] Guoping Dong,[†] Shifeng Zhou,[†] Qinyuan Zhang,[†] Zhongmin Yang,[†] and Jianrong Qiu*[,†]

[†]State Key Laboratory of Luminescent Materials and Devices, South China University of Technology, Wushan Road No. 381, Tianhe District, Guangzhou 510640, China

[‡]School of Materials Science and Engineering, South China University of Technology, Wushan Road No. 381, Tianhe District, Guangzhou 510640, China

Supporting Information

ABSTRACT: Structural design of photocatalysts is of great technological importance for practical applications. A rational design of architecture can not only promote the synthetic performance of photocatalysts but also bring convenience in their application procedure. Nanofibers have been established as one of the most ideal architectures of photocatalysts. However, simultaneous optimization of the photocatalytic efficiency, mechanical strength, and thermal/chemical tolerance of nanofibrous photocatalysts remains a big challenge. Here, we demonstrate a novel design of TiO_2–SiO_2 composite fiber as an efficient photocatalyst with excellent synthetic performance. Core–shell mesoporous SiO_2 fiber with high flexibility was employed as the backbone for supporting ultrasmall TiO_2 nanowhiskers of the anatase phase, constructing core@double-shell fiber with luffa-sponge-like appearance. Benefitting from their continuously long fibrous morphology, highly porous structure, and completely inorganic nature, the TiO_2–SiO_2 composite fibers simultaneously possess high photocatalytic reactivity, good flexibility, and excellent thermal and chemical stability. This novel architecture of TiO_2–SiO_2 glass composite fiber may find extensive use in the environment remediation applications.

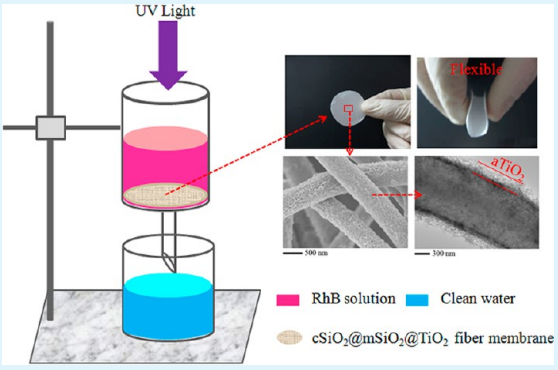

KEYWORDS: *TiO_2 nanowhisker, SiO_2 glass fiber, electrospinning, photocatalyst, water purification*

1. INTRODUCTION

Photocatalytic decomposition is one of the most efficient approaches for eliminating air or water pollutants. In the last decades, a plethora of investigations have been paid to TiO_2 (titanium dioxide) as an efficient photocatalyst, because of its acceptable photocatalytic activity, high chemical stability, low cost, non-toxicity, and diverse preparation methods.[1−6] In addition, TiO_2 has been proved to be environmentally friendly and biocompatible. Although TiO_2 has been recognized as the most promising photocatalyst, many remaining challenges, mainly including further improvement of the catalytic efficiency and the separation and reclaiming of photocatalysts from the environment, still should be concerned for practical applications. Diminishing particle size and increasing specific surface area are very efficient and extensively applied scenarios for enhancing the catalytic efficiency of the photocatalysts.[7] Therefore, nanosize TiO_2 of diverse architectures have been created, for example, the commercially available Degussa P25 TiO_2 nanopowder (hereafter written as P25 for convenience). Decrease of particle size, on one hand, can increase the surface-to-volume ratio of TiO_2 and enhance the photocatalytic ability. However, ultrasmall particles, on the other hand, also make the separation process quite difficult, which will inevitably cause secondary pollution. Besides, the high surface energy also leads to easy aggregation of ultrasmall TiO_2 nanoparticles.

Assembling TiO_2 nanoparticles/nanostructures into macroscopic architectures has been extensively studied, in order to create photocatalysts with both high photocatalytic reactivity and ease of separation.[8−10] Another effective way to simultaneously improve the photocatalytic reactivity and separation convenience is to introduce nanoporous structures in the TiO_2 matrix.[11−13] Recently, a versatile electrospinning technique was extensively investigated to fabricate fibrous TiO_2 with diameters ranging from nano- to microscale.[14−18] The obtained TiO_2 fibers usually possess a high catalytic ability, and their fibrous macroconfiguration also makes the separation and reclaiming very simple. However, their polycrystalline nature always causes poor mechanical strength, seriously restricting their applications. Immobilizing nano-TiO_2 with supporting materials, such as polymer matrix, zeolite, carbon, or

Received: May 15, 2013
Accepted: July 17, 2013
Published: July 17, 2013

mesoporous silica, is also an effective way to avoid aggregation of nano-TiO_2, and simplify the separation and reclaiming procedure.[19−26] Nevertheless, in a lot of reported research, the immobilization of TiO_2 nanoparticles, for example, direct embedding in a polymer matrix,[19] made a large part of the particles inaccessible in use, which seriously decreased the photocatalytic efficiency. A better immobilization method is still needed to be developed without a decrease or even with an increase of the catalysts' efficiency.

Commercially available polymer fibers, especially cotton fibers, are investigated by many researchers for their surface grafting of TiO_2 nanoparticles, in order to realize photocatalysis-assisting self-cleaning functionality.[27−29] However, thick fibers are not ideal for environmental purification, due to the relatively low specific surface area. Very recently, J. A. Lee et al.[30] reported the grafting of ultrasmall TiO_2 nanoparticles of anatase phase on the surface of electrospun polymer fibers at room temperature using a LBL (layer-by-layer) method. They used POSS−NH^{3+} (octa(3-ammoniumpropyl)-octasilsesquioxane octachloride) to prevent the UV irradiation induced decomposition of the polymer matrix. Such TiO_2-nanoparticle-decorated polymer fibers were highly reactive and at the same time retained the fibers' flexibility, possessing wide applications. The flexible fibers could be conveniently made into porous film for environmental remediation through filtration and UV irradiation. However, some shortcomings still exist. The poor thermal resistance of the polymer fibers made their remediation from stubborn organic contamination (organic dust or microorganisms deposited on the film) very difficult. Besides, the deposited TiO_2 nanoparticles stacked closely, decreasing the accessibility of the inner-layer TiO_2 nanoparticles. In another aspect, SiO_2 nanofibers derived from sol-gel and electrospinning techniques possess excellent chemical/thermal stability, high flexibility, and big surface area. They have been widely investigated for supporting many kinds of ceramic nanostructures, including TiO_2 nanoparticles.[31−33] However, the optimization for performance of the SiO_2−TiO_2 composite fibers is still far from enough.

Herein, we propose a novel design of TiO_2−SiO_2 composite fiber as efficient photocatalyst. We used flexible SiO_2 glass fiber as the scaffold for supporting ultrasmall TiO_2 nanocrystals. Submicrometer SiO_2 glass fiber was prepared using the sol-gel and electrospinning techniques, then cladded with a mesoporous SiO_2 shell through a modified Stöber method to form a core−shell architecture. After thermal treating in an autoclave and subsequent reaction, the core−shell fiber was muffled with a layer of porous network composed of ultrasmall TiO_2 nanowhiskers, constructing a core@double-shell architecture. As a photocatalyst, this kind of composite fiber possesses several advantages: (1) Its dual porous structure endows it with a huge specific surface area, which is especially beneficial to improve the catalytic efficiency. (2) The mesoporous SiO_2 shell can act as an adsorbent for pre-concentrating the pollutants, which also promotes the removal efficiency of pollutants. (3) The fibers possess a high flexibility and excellent thermal stability. They can be compiled into hierarchically porous film easily with wide-spread use. (4) The completely inorganic nature promises great convenience in their remediation from organic pollution via simple calcination. These characters are quite important in practical applications. According to the structural characters of the fiber (core of condensed SiO_2 fiber ($cSiO_2$), mediate shell of mesoporous SiO_2 ($mSiO_2$), and outer shell of TiO_2 nanowhiskers), it is nominated as $cSiO_2$@$mSiO_2$@TiO_2. The water purification ability of the $cSiO_2$@$mSiO_2$@TiO_2 was evaluated with RhB (rhodamine B) and commercial P25 as the model organic pollutant and reference, respectively.

2. EXPERIMENTAL SECTION

Preparation of $cSiO_2$@$mSiO_2$@TiO_2 Fibers. $cSiO_2$@$mSiO_2$ fibers (please refer to our previous research[34]) (0.2 g) were placed in a small basket made of 180 mesh stainless steel screen, which was fixed above liquid $TiCl_4$ (titanium tetrachloride, 5 mL) contained in a 60 mL Teflon-lined autoclave. Filling of $TiCl_4$ into the mesopores of the fibers was carried out by heating the autoclave at 130 °C for 20 h under autogenous pressure. After the autoclave cooled to room temperature, the fibers together with the small basket were picked out and exposed in air for 1 h. In this stage, a lot of smog could be observed fuming out of the fibers. The fibers were then transferred into an oven and dried at 90 °C followed by calcination at 500 °C in a muffle furnace for 3 h to generate the final $cSiO_2$@$mSiO_2$@TiO_2 fibers.

Preparation of $cSiO_2$@$mSiO_2$@TiO_2 Film. Hierarchically porous film composed of $cSiO_2$@$mSiO_2$@TiO_2 fibers was prepared on the basis of modification of the method applied to fabricate $cSiO_2$@$mSiO_2$@TiO_2 fibers, as described above. Briefly, $cSiO_2$@$mSiO_2$ fibers (0.12 g) were gently dispersed homogeneously in deionized water (50 mL). Then, the fiber suspension was poured slowly into a stainless steel basket (its diameter at the bottom was 3.2 cm), and the fibers were deposited on the steel screen to make a disk-shaped nonwoven film. The following steps were the same as that for preparation of $cSiO_2$@$mSiO_2$@TiO_2 fibers. For convenience, the film prepared here was called $cSiO_2$@$mSiO_2$@TiO_2 film.

Characterization. Micro-morphologies of the samples were characterized by SEM (scanning electron microscopy, Hitachi S-4800) and TEM (transmission electron microscopy, Philips CM 200UT); crystalline structures of the samples were investigated using XRD (X-ray diffraction, RIGAKU D/MAX 2550/PC); the porosity of the samples was studied through N_2 adsorption−desorption experiment (Quantachrome, AUTOSORB-1-C); the surface area of TiO_2 nanowhiskers derived from dissolving the SiO_2 of the $cSiO_2$@$mSiO_2$@TiO_2 fibers (here named as TNWs) was also investigated with N_2 adsorption−desorption isotherms; FTIR spectra (Fourier transform infrared spectroscopy) of the samples were measured with a Bruker Vector 33 FTIR spectrophotometer.

To investigate the adsorption kinetics of RhB on $cSiO_2$@$mSiO_2$@TiO_2 fibers and P25, $cSiO_2$@$mSiO_2$@TiO_2 fibers (0.2 g) or P25 (0.2 g) were dispersed in an aqueous solution of RhB (100 mL) with a concentration of 24 $mg{\cdot}L^{-1}$. At selected time intervals, aliquots (2 mL) were extracted, immediately mixed with deionized water (8 mL), and filtrated for measuring the concentration of remaining RhB with an UV−vis/IR spectrophotometer. To evaluate the adsorption capacity of RhB on the $cSiO_2$@$mSiO_2$@TiO_2 fibers or P25, $cSiO_2$@$mSiO_2$@TiO_2 fibers (0.01 g) or P25 (0.01 g) were dispersed in RhB solution (10 mL) with gradient concentrations and the mixture was magnetically stirred in the dark under room temperature for 3 h. Then, the solid was filtered away and the solution was kept for measuring the concentration of the remaining RhB.

The photocatalytic performance of the samples was evaluated using a home-made setup, with Degussa P25 as a reference. A 300 W Osram Ultra-Vitalux UV light (the luminescent spectrum of this light was shown in Figure S1, Supporting Information) was used as the light source during the whole photocatalysis procedure. The distance from the bottom of the light to the surface of the RhB−photocatalyst suspension was kept constantly at 12 cm, and the light power at the surface of the reaction solution was measured to be about 735 $mW{\cdot}cm^{-2}$ (at a wavelength of 365 nm, measured with a Thor Labs, PM320 dual-channel optical power and energy meter). To monitor the photocatalytic degradation of the pollutant along with the irradiation time, P25 + $cSiO_2$@$mSiO_2$ (0.09 g of P25 and 0.31 g of $cSiO_2$@$mSiO_2$) or $cSiO_2$@$mSiO_2$@TiO_2 fibers (0.4 g, equivalent mass of TNWs was 0.09 g) or TNWs + $cSiO_2$@$mSiO_2$ (0.09 g of TNWs and

Figure 1. Schematic demonstration for the preparation procedure of the $cSiO_2@mSiO_2@TiO_2$ fibers. $TiCl_4$ was thermally pressed into the pores of the mesoporous SiO_2 shell and then escaped from the pores and was hydrolyzed by the air moisture and generated the precursor of TiO_2 nanowhiskers. After calcination in air, the final $cSiO_2@mSiO_2@TiO_2$ fibers were created.

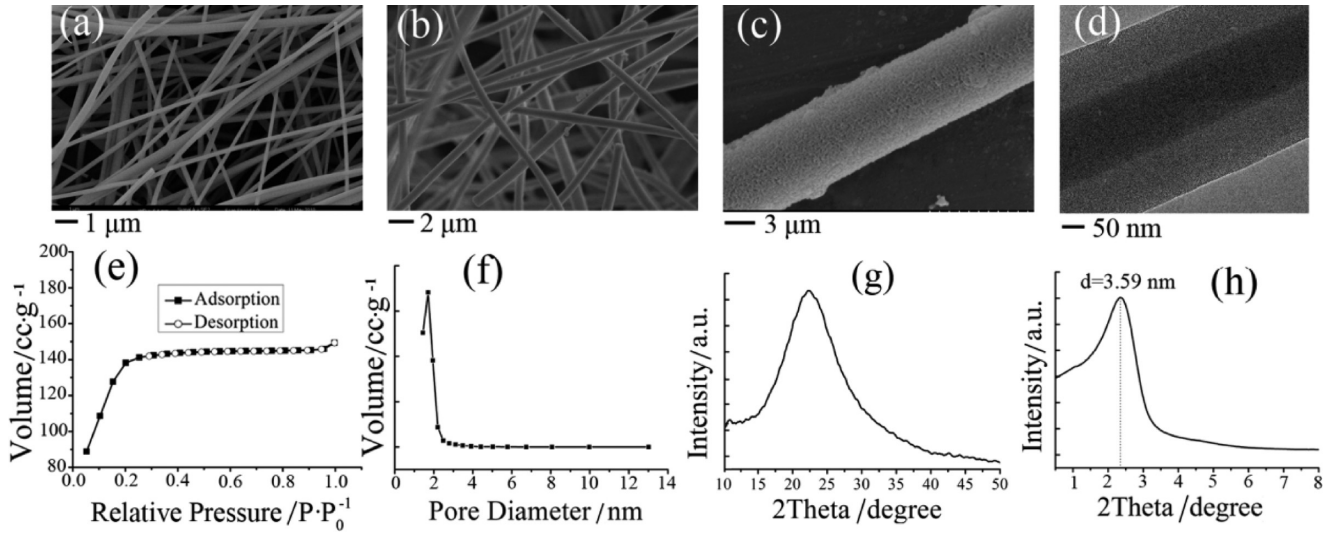

Figure 2. SEM images of (a) electrospun $cSiO_2$ fibers and (b) $cSiO_2@mSiO_2$ fibers; (c) high-magnification SEM image of a single $cSiO_2@mSiO_2$ fiber; (d) TEM image of a single $cSiO_2@mSiO_2$ fiber; (e) N_2 adsorption−desorption isotherm curves of $cSiO_2@mSiO_2$ fibers; (f) pore-diameter distribution curve of $cSiO_2@mSiO_2$ fiber calculated according to the N_2 adsorption isotherm; (g, h) XRD and SAXRD (small-angle XRD) patterns of $cSiO_2@mSiO_2$ fibers.

0.31 g of $cSiO_2@mSiO_2$), P25 (0.1 g), or TNWs (0.1 g) were dispersed in deionized water (50 mL) under magnetic stirring to form solution A. Then, RhB (120 mg) was dissolved in deionized water (50 mL) contained in a circulating-water-cooled glass beaker to form solution B. The reaction system was fixed in a steel box to avoid natural light. Once solutions A and B were mixed together, the time was recorded. Before irradiation, the mixed suspension was stirred in the dark for 1 h to ensure saturated adsorption of RhB on the catalysts. During the irradiation stage, aliquots (2 mL) of the suspension were extracted at selected time intervals and immediately mixed with 8 mL of deionized water, and then filtrated to get a transparent solution for measuring the relative concentration of the remaining RhB. The experimental conditions in the whole photocatalysis procedure, including the environmental temperature, the distance from the UV light to the surface of the reaction solution, etc., were kept constant. To investigate whether visible light contributes to the photocatalytic decomposition of RhB with the $cSiO_2@mSiO_2@TiO_2$ fibers or P25 as photocatalyst, a Solar-500 Xenon lamp was used as the light source to replace the UV light and wavelengths shorter than 420 nm were filtered by a long-pass filter in the experiment.

Demonstration for removing organic pollutant from water using the $cSiO_2@mSiO_2@TiO_2$ film was implemented also with a home-made setup, as schematically illustrated in Figure S2 (Supporting Information). The $cSiO_2@mSiO_2@TiO_2$ film (size: diameter and thickness relatively being 3.2 cm and 0.4/0.7/1.0 mm) was fixed at the bottom of a glass tube and supported by a 180-mesh stainless steel screen. RhB−water solution (20 mL) with varied concentrations was slowly poured into the glass tube; then, the UV irradiation began until all of the solution passed through the film. The distance from the bottom of the light to the surface of the film was kept constant at about 8 cm, and the light power at the surface of the film was about 1.73 $W \cdot cm^{-2}$ (at a wavelength of 365 nm). The RhB concentration of the tested solutions was measured with a UV−vis/IR spectrophotometer in the whole experiment.

To evaluate the regeneration ability of the film composed of $cSiO_2@mSiO_2@TiO_2$ fibers, water blooms separated from lake water were used as a model organic pollutant. After photocatalysis of RhB solution with the clean film, a certain quantity of water blooms dispersed in deionized water (5 mL) were poured onto the film. Then, the film was shifted into a drying oven once it stopped dripping. The thoroughly dried film was investigated for its photocatalytic removal efficiency of RhB under the same condition as the clean film was. The concentration of RhB solution used here was kept at 6 $mg \cdot L^{-1}$.

3. RESULTS AND DISCUSSION

In our previous research,[34] core−shell structured mesoporous SiO_2 fibers were synthesized via a modified Stöber method using electrospun SiO_2 nanofiber as a soft template, which we named $cSiO_2@mSiO_2$. Such glassy fiber possesses several unique priorities, including high chemical and thermal stability, easy colloidal-forming ability, huge specific surface area, and good flexibility. These advantages endow this material with great potential for various applications. For example, our recent

dx.doi.org/10.1021/am401827k | ACS Appl. Mater. Interfaces 2013, 5, 7527−7536

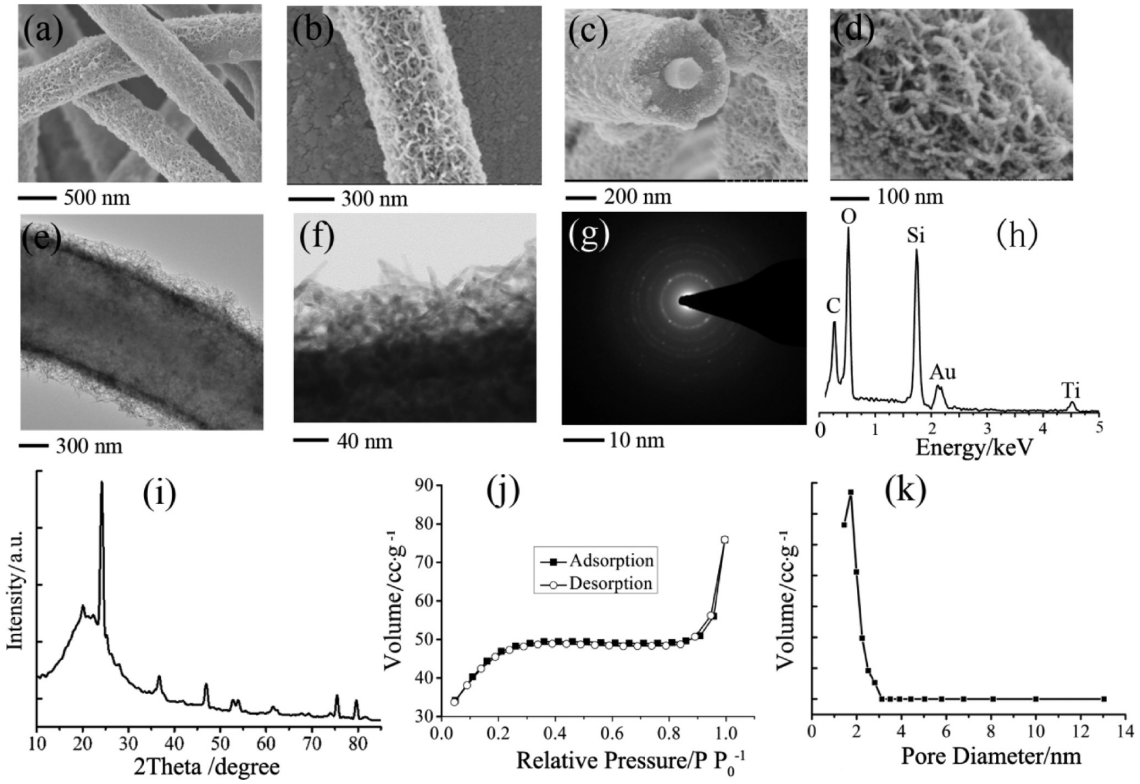

Figure 3. (a) SEM image of $cSiO_2@mSiO_2@TiO_2$ fibers; (b, c) SEM images of one single $cSiO_2@mSiO_2@TiO_2$ fiber with side and tip view, respectively; (d) magnified SEM image of the surface morphology of $cSiO_2@mSiO_2@TiO_2$ fiber; (e, f) TEM images of $cSiO_2@mSiO_2@TiO_2$ fiber under different magnifications; (g–i) SAED (selected area electron diffraction), EDX (energy dispersive X-ray diffraction), and XRD pattern of $cSiO_2@mSiO_2@TiO_2$ fiber; (j, k) N_2 adsorption–desorption isotherm curves of $cSiO_2@mSiO_2@TiO_2$ fibers, and corresponding pore-size distribution curve calculated due to the N_2 desorption isotherm.

investigation had demonstrated the successful application of the $cSiO_2@mSiO_2$ fiber for water purification.[34] The mesoporous fibers could efficiently remove heavy metal ions from water. Besides, their high flexibility makes them easy to be patterned into porous film, consequently extending their applicability. Considering the characters of good photocatalysts, especially for water purification, namely, high photocatalytic efficiency, easy separation, recycling process, etc., we envisage that the $cSiO_2@mSiO_2$ fibers may find wide use in photocatalytic applications, if photocatalyst (such as TiO_2) can be integrated in a rational manner. Balkus et al.[35−37] reported a very simple and versatile method for preparation of TNWs using mesoporous silica (DAM-1) as a template. Volatile $TiCl_4$ was thermally pressed into the mesopores of DAM-1 under autogenous pressure in a heated autoclave. When escaping from the meopores into air at room temperature, the $TiCl_4$ vapor was hydrolyzed by the moisture, generating precursor TNWs, which were then converted to final TNWs by calcination. In this investigation, we synthesized $cSiO_2@mSiO_2@TiO_2$ in a similar approach. Figure 1 schematically illustrates the preparation procedure of the $cSiO_2@mSiO_2@TiO_2$ fibers. Condensed SiO_2 nanofibers were first prepared through the sol-gel and electrospinning techniques. Then, the as-spun SiO_2 nanofibers were cladded with a mesoporous SiO_2 shell through a modified Stöber method using CTAB as the pore-forming surfactant and subsequent calcination. The excellent chemical and thermal stability of the SiO_2 glass nanofibers made it feasible to conduct thermal treating in an autoclave containing $TiCl_4$ together with hydrolysis in air and calcination to generate the final fibers decorated with TNWs of the anatase phase.

As shown in Figure 2a, the electrospun SiO_2 nanofibers exhibit a continuously long fibrous morphology with an average diameter around 240 nm. After post-treating with a modified Stöber method, the as-spun fibers were cladded with a layer of porous shell while retaining their long fibrous morphology very well (Figure 2b,c). Their average diameter increased to more than 460 nm. The core–shell structure and porous shell of the fibers are clearly established by the TEM image (Figure 2d). The porosity of the sample was evaluated with N_2 adsorption–desorption isotherms. The core–shell SiO_2 fiber presents an I type isotherm without obvious hysteresis loops, indicative of a highly uniform pore size (Figure 2e). The specific surface area and total pore volume of the sample were calculated to be 391 $m^2 \cdot g^{-1}$ and 0.164 $cm^3 \cdot g^{-1}$, respectively. The pore size distribution curve presents a very narrow shape with a sharp peak at 2 nm, also demonstrating the high uniformity of the mesopores (Figure 2f). The average diameter of the mesopores was calculated to be 2.57 nm. Due to the XRD results (Figure 2g,h), the core–shell fiber presents an amorphous structure, and diffraction originated from the periodic porous structure of the shell is demonstrated clearly. Accordingly, the cell diameter of the mesopores is determined to be about 3.59 nm, and the wall thickness of the mesopores is calculated to be 0.5 nm.

The tolerant mesoporous SiO_2 shell of the $cSiO_2@mSiO_2$ fibers provided a host for incorporation of $TiCl_4$ under rigorous thermal pressing conditions, making the loading of TiO_2 nanophotocatalyst possible. During the procedure for loading TNWs, dry $cSiO_2@mSiO_2$ fibers were fixed above the surface

of liquid $TiCl_4$, which was contained in a sealed autoclave. Then, the elevated temperature accelerated the evaporation of the $TiCl_4$, which created a very high vapor pressure of $TiCl_4$ around the SiO_2 fibers. As a result, the $TiCl_4$ vapor invaded into the mesopores of the fibers, and liquefied in the pores after the temperature restored to room temperature. Once exposed in the air, where the vapor pressure of $TiCl_4$ was much lower than in the autoclave, the incorporated $TiCl_4$ in the mesopores evaporated again, escaped from the pores, and was hydrolyzed by the moisture in the air, generating the precursor TNWs. After calcination, the final $cSiO_2@mSiO_2@TiO_2$ fibers were created. As shown by the SEM images (Figure 3a–d), the $cSiO_2@mSiO_2$ fibers were muffled by a layer of very small nanowhiskers, which interconnected with each other, constructing a porous network on the fibers' surface, making the fibers appear like a luffa sponge. The magnified SEM image (Figure 3d) revealed the micro-morphology of the nanowhiskers much clearer. Each nanowhisker was composed of several stringed nanoparticles, forming a polycrystalline structure. TEM images (Figure 3e,f) revealed the inner structure of the composite fiber. Three layers can be distinguished: the condensed electrospun SiO_2 fiber with medium contrast at the core, then the mesoporous SiO_2 with low contrast forming the middle layer, and the crystalline nanowhiskers with high contrast being the outer sheath. From the TEM images, the porous network of the nanowhisker layer can be observed quite clearly; a lot of interconnecting voids exist among the nanowhiskers. The mean diameter of the TNWs was measured to be 11 nm. Such ultrasmall particle size is very beneficial to improve the reactivity of TiO_2. By employing SAED (selected area electron diffraction, Figure 3g) analysis, the nanowhiskers covering the surface of the fibers were identified to be polycrystalline TiO_2 of the anatase phase, which has demonstrated the best catalytic ability among all the mono-crystalline phases of TiO_2. By EDS analysis, as shown in Figure 3h, the mass ratio of TiO_2 of the $cSiO_2@mSiO_2@TiO_2$ fiber was determined to be about 22.3%. The XRD pattern in Figure 3i further identifies the crystalline phase of the sample; besides the broadened diffraction peak of amorphous SiO_2 at about $2\theta = 22°$, all the diffraction peaks from anatase TiO_2 can be clearly discerned. After muffling of the TNWs, N_2 adsorption–desorption isotherms of the sample remained to be the same type (type I, as shown in Figure 3j) as $cSiO_2@mSiO_2$, with its pore-size-distribution curve varied slightly (Figure 3k). The peak center shifted to smaller diameter (about 1.74 nm), and the mean diameter of the mesopores decreased to less than 2 nm. The specific surface area and pore volume of the sample decreased to 160 $m^2 \cdot g^{-1}$ and 0.117 $cc \cdot g^{-1}$, respectively. Table 1 summarizes the N_2 adsorption–desorption results of the samples before and after growth of the TNWs. From the N_2 adsorption–desorption results and the TEM image in Figure 3e, we deduce that some of the mesopores of the sample (especially in the outer layer) have been filled by the TiO_2, but some were still bare without blockage. During the thermal pressing of $TiCl_4$, the capillary force in the nanopores increased with decrease of the pore diameter. Consequently, it was much easier for the $TiCl_4$ vapor to invade into those relatively big pores during the thermal pressing stage. As a result, for the final $cSiO_2@mSiO_2@TiO_2$ fibers, perhaps most of the relatively big pores, were blocked by TiO_2, while the relatively small pores were still open, which led to a decrease of the mean pore size and surface area. Of course, to determine the precise minimum pore diameter, above which $TiCl_4$ can be pressed into the pores under certain experimental conditions, is not the scope of this investigation. From the N_2 adsorption–desorption results, it can be determined that the N_2 gas could penetrate through the TNW layer into the middle mesoporous SiO_2 shell, implying that the whole layer of TNWs possessed a highly porous structure. For photocatalytic water purification, such a porous structure is quite beneficial; this will be demonstrated in the following discussion. The porosity of the TNW layer of the $cSiO_2@mSiO_2@TiO_2$ fibers was also studied via N_2 adsorption–desorption. As shown in Figure 4, the TNWs presented a III type N_2 adsorption–desorption isotherm with a very slim H4 type hysteresis loop. The surface area of the TNWs was calculated to be 121 $m^2 \cdot g^{-1}$.

Table 1. N_2 Adsorption Desorption Results of the Samples

sample	BET surface area ($m^2 \cdot g^{-1}$)	pore volume ($cm^3 \cdot g^{-1}$)	pore size (nm)
$cSiO_2@mSiO_2$	391	0.164	2.57
$cSiO_2@mSiO_2@TiO_2$	160	0.117	2
TNWs	121		

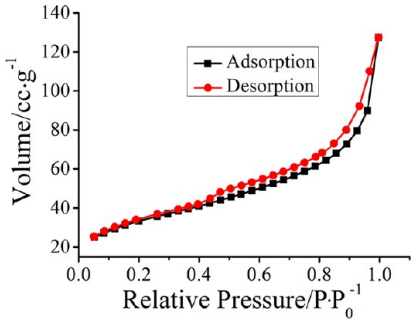

Figure 4. N_2 adsorption–desorption isotherms of the TNWs (TiO_2 nanowhiskers derived by dissolution of the SiO_2 component of the $cSiO_2@mSiO_2@TiO_2$ fibers).

In the hydrolysis stage of $TiCl_4$, the room humidity played an important role that influenced the micro-morphology of the fibers. As presented in Figure 5a–c, along with the increase of the room humidity, the whisker-like morphology of the TiO_2 nanoparticles became more and more fuzzy. The root segment of the TNWs began to merge when the humidity increased to 55–65%, and complete merging occurred when the humidity increased to higher than 75%. Consequently, a relatively low room humidity was required to fabricate $cSiO_2@mSiO_2@TiO_2$ fibers with fine TNWs. Besides the room humidity during the hydrolysis stage, the distance between the $cSiO_2@mSiO_2@TiO_2$ fibers and the liquid level of $TiCl_4$ in the thermal pressing stage also influenced the morphology of the final sample seriously. When this distance was bigger than 5 cm, only very small nanoparticles were generated, as shown by Figure 5d1 (the distance was about 5.2 cm). After such distance was narrowed to about 4 cm, small rod-shaped TiO_2 particles with low aspect ratio (mean length, 28 nm; average aspect ratio, 1.93) began to emerge (Figure 5e1); while the distance decreased to 2.5 cm (Figure 5f1), fine TNWs were obtained finally. Parts d2–f2 of Figure 5 present the EDS patterns of the samples corresponding to Figure 5d1–f1. The mass ratios of TiO_2 of the three samples were measured to be 10.12, 18.12, and 22.3 wt %, respectively. Consequently, a relatively small distance between the fibers and the liquid level of $TiCl_4$ was

dx.doi.org/10.1021/am401827k | ACS Appl. Mater. Interfaces 2013, 5, 7527–7536

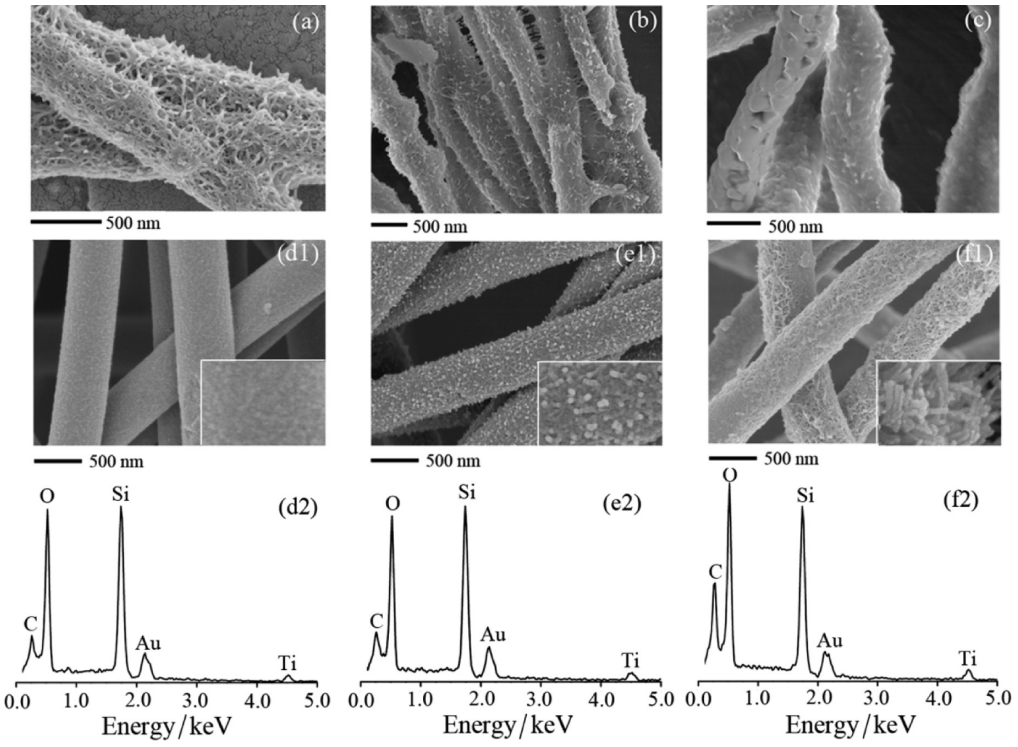

Figure 5. (a–c) SEM images of $cSiO_2@mSiO_2@TiO_2$ fibers derived with different hydrolyzing humidity (the corresponding humidities for parts a–c were 35–45%, 55–65%, and 75–85%, respectively); (d1–f1) SEM images of $cSiO_2@mSiO_2@TiO_2$ fibers derived with different distances between the liquid $TiCl_4$ surface to the supported $cSiO_2@mSiO_2$ fibers during the thermal pressing process of $TiCl_4$ (the corresponding distance for parts a1–c1 were 5.2, 4, and 2.5 cm, respectively); (d2–f2) EDX patterns corresponding with parts d1–f1.

beneficial for growth of whisker-like TiO_2 crystals. We believe the distance-related morphological variation should be ascribed to the gradient distribution of the vapor pressure from the liquid surface to the top part of the Teflon container. Other factors that could affect the fiber's morphology, especially the pore size of the porous SiO_2 sheath, have been reported by Balkus et al. on particulate mesoporous silica materials;[35,36] they are not the scope of this investigation.

We used RhB, an extensively used dye (whose molecular structure is presented in Figure S3, Supporting Information), as a model organic pollutant to evaluate the photocatalytic ability of the $cSiO_2@mSiO_2@TiO_2$ fibers. Before irradiation with UV light, the evaluation system was placed in the dark with gentle magnetic stirring for 1 h to ensure saturated adsorption of the organics on the catalysts. Figure 6 shows the photocatalytic degradation of RhB under UV light along with irradiation time.

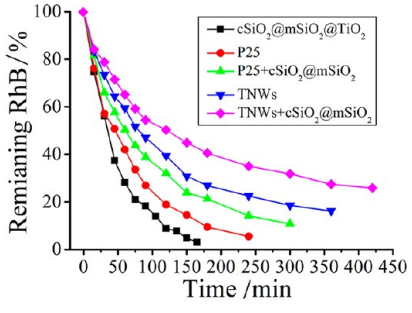

Figure 6. Kinetics of the photocatalytic decomposition of RhB under UV irradiation and with $cSiO_2@mSiO_2@TiO_2$ fibers (black line), Degussa P25 (red line), P25 + $cSiO_2@mSiO_2$ fibers (green line), TNWs (blue line), and TNWs + $cSiO_2@mSiO_2$ fibers as catalysts.

P25 + $cSiO_2@mSiO_2$ (0.09 g of P25 and 0.31 g of $cSiO_2@mSiO_2$), $cSiO_2@mSiO_2@TiO_2$ fibers (0.4 g), or TNWs + $cSiO_2@mSiO_2$ (0.09 g of TNWs and 0.31 g of $cSiO_2@mSiO_2$) were separately dispersed in 100 mL of aqueous solution containing 120 mg of RhB for comparative investigation. Among these three sorts of catalysts, the $cSiO_2@mSiO_2@TiO_2$ fibers exhibited the most efficient photocatalytic ability; more than 95% decomposition of RhB was achieved within 150 min (the black curve). The P25 + $cSiO_2@mSiO_2$ showed medium reactivity; about 90% RhB was decomposed within 300 min (the green curve). The TNWs + $cSiO_2@mSiO_2$ presented the poorest photocatalytic ability; only less than 75% RhB removal efficiency was achieved during 420 min photocatalytic reaction (the purple curve). We also investigated the removal of RhB with P25 or TNWs as photocatalyst. As shown by the red and blue curves in Figure 6, without the addition of $cSiO_2@mSiO_2$, both TNWs and P25 presented faster decomposition of RhB than their $cSiO_2@mSiO_2$-added counterparts, and the reactivity of P25 was higher than that of TNWs. Addition of the $cSiO_2@mSiO_2$ fibers would increase the light diffraction during the photocatalysis process, which could bring about two consequences: on one hand, it could enhance the photo-absorption probability by the photocatalyst within the depth where the light could penetrate, which was beneficial to improve the photocatalysis efficiency and should be termed as a positive effect; on the other hand, the increased light diffraction also could lead to a decrease of the light penetration depth itself, which degraded the photocatalysis efficiency and should be termed as a negative effect. Consequently, the final effect of addition of the $cSiO_2@mSiO_2$ fibers depended on whether the positive or negative effect played the dominant role in the photocatalysis process. From the above discussion, it can be

deduced that, for both P25 and TNWs, the negative effect stemming from the addition of $cSiO_2@mSiO_2$ fibers dominated in the photocatalysis experiment. As a result, their photocatalytic efficiency decreased, compared with their counterparts without the addition of $cSiO_2@mSiO_2$ fibers. Table 2 lists the

Table 2. Decomposition Rate of RhB with Different Photocatalysts

sample	RhB decomposition rate ($\mu g \cdot min^{-1}$)
$cSiO_2@mSiO_2@TiO_2$	710
P25 + $cSiO_2@mSiO_2$	360
TNWs + $cSiO_2@mSiO_2$	210
P25	470
TNWs	280

decomposition rates of RhB with different photocatalysts. While using a xenon lamp as the light source (wavelength >420 nm), no decomposition of RhB was observed with all of the above photocatalysts (results are not given here).

From the above results, it can be concluded that, for the photocatalytic removal of RhB from water, the $cSiO_2@mSiO_2@TiO_2$ fibers were more efficient than the TNWs + $cSiO_2@mSiO_2$ and the P25 + $cSiO_2@mSiO_2$, while P25 showed a higher reactivity than TNWs. This phenomenon indicated that the interfacial interaction between the TNWs and the $cSiO_2@mSiO_2$ of the $cSiO_2@mSiO_2@TiO_2$ fibers played a very important role in improving the photocatalysis efficiency. We specify the detailed mechanism as follows: (i) The highly reactive anatase phase of the TNWs and their ultrathin diameter endowed the $cSiO_2@mSiO_2@TiO_2$ fibers with high catalytic reactivity. Besides, the TNWs were fixed on the SiO_2 fibers, which effectively avoided their agglomeration and consequently alleviated or even inhibited the degradation of their reactivity stemming from agglomeration. (ii) The TNWs interconnected together, forming a porous luffa-sponge-like network. Meanwhile, the mediate SiO_2 shell also was highly porous. Stacking of the dual porous $cSiO_2@mSiO_2@TiO_2$ fibers generated a hierarchically porous structure, which tremendously enhanced the accessibility of the reactive sites during the photocatalysis process.[34,38] (iii) Although covered by the TNW layer, a large part of the surface of the mesoporous SiO_2 shell was still accessible, due to the porous structure of the TiO_2 layer. The huge surface area (this was identified by the N_2 adsorption−desorption isotherms of the sample, as discussed above) of the SiO_2 fiber made it able to abundantly grab the RhB molecules in water and gather the organic pollutants around the neighboring area of the TNWs, thus remarkably accelerating the photocatalysis procedure. This can be proved by the adsorption kinetics and isotherms of RhB on the $cSiO_2@mSiO_2@TiO_2$ fibers and the P25, as presented in Figure 7a−d. Saturated adsorption of RhB on $cSiO_2@mSiO_2@TiO_2$ fibers was achieved within 5 min, and the maximum adsorption capacity was calculated to be 132 $mg \cdot g^{-1}$, according to the isotherm curves. The corresponding time for saturated adsorption of RhB on P25 was almost at the same scale; however, the maximum adsorption capacity decreased to 3.4 $mg \cdot g^{-1}$. This suggests that, during the photocatalysis procedure, the organic pollutants in water could be massively preconcentrated near the TNWs of the $cSiO_2@mSiO_2@TiO_2$ fibers with a much higher capacity than P25, which provided more opportunity for the RhB molecules to be decomposed under UV irradiation. FTIR spectra of the sample and P25 after the adsorption experiments were recorded to further compare their adsorption ability (the initial concentration of the corresponding RhB solution was 120 mg/L). As shown by curve b in Figure 7e, besides the characteristic absorption peaks from the $cSiO_2@mSiO_2@TiO_2$ fibers, vibration peaks from

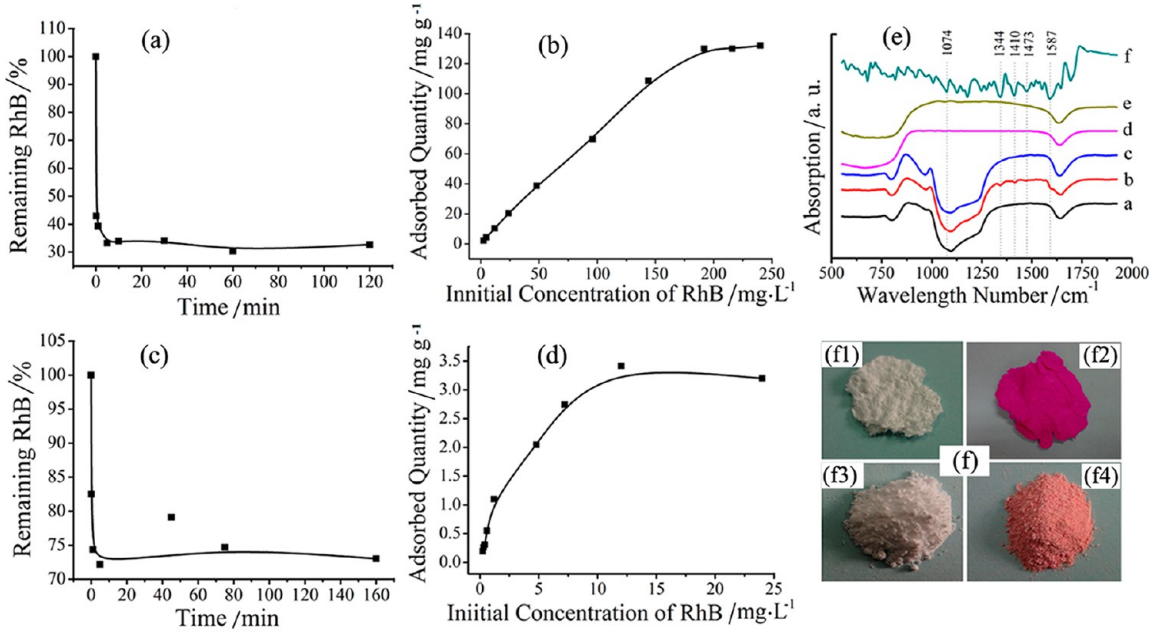

Figure 7. (a, b) Adsorption kinetics and isotherm of RhB on $cSiO_2@mSiO_2@TiO_2$ fibers; (c, d) adsorption kinetics and isotherm of RhB on Degussa P25; (e) FTIR spectra of $cSiO_2@mSiO_2@TiO_2$ fibers before and after saturated adsorption of RhB (lines a and b), $cSiO_2@mSiO_2@TiO_2$ fibers filtered from the solution after completion of the photocatalysis reaction (line c), Degussa P25 before and after saturated adsorption of RhB (lines d and e) and RhB used in this investigation (line f); (f1, f2) digital images of $cSiO_2@mSiO_2@TiO_2$ fibers before and after saturated adsorption of RhB; (f3, f4) digital images of Degussa P25 before and after saturated adsorption of RhB.

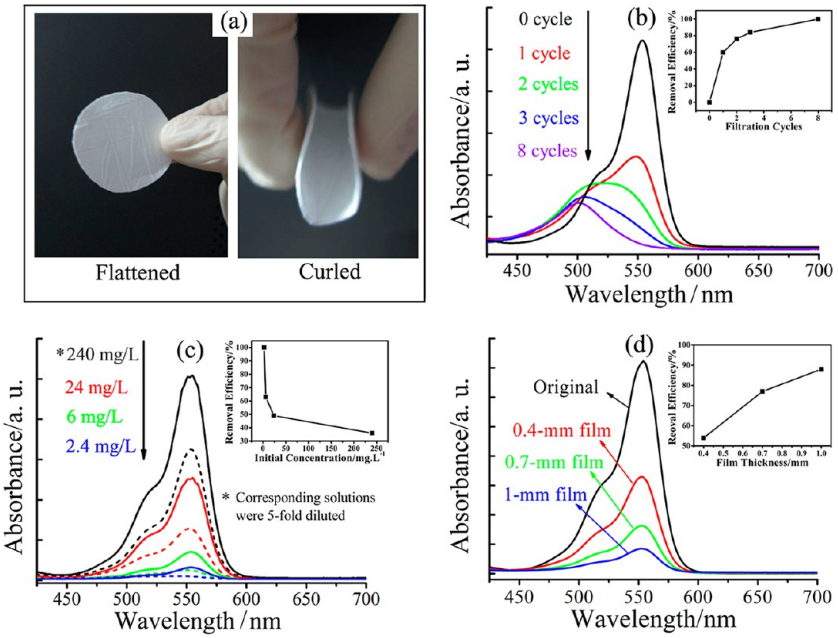

Figure 8. (a) Digital images of nonwoven film composed of $cSiO_2@mSiO_2@TiO_2$ fibers in flattened and curled status, respectively; (b) absorption spectra of RhB solution (RhB concentration: 6 mg·L^{-1}) after different circles of filtration with $cSiO_2@mSiO_2@TiO_2$ film (thickness: 0.7 mm) accompanied by UV irradiation; (c) absorption spectra of RhB solution with various concentrations before (solid lines) and after (dashed lines) one cycle of filtration with $cSiO_2@mSiO_2@TiO_2$ film (thickness: 0.7 mm) accompanied by UV irradiation; (d) absorption spectra of RhB solution (RhB concentration: 6 mg·L^{-1}) after filtration with $cSiO_2@mSiO_2@TiO_2$ film of different thickness accompanied by UV irradiation.

RhB, including 1344, 1410, 1473, and 1587 cm^{-1}, can be discerned clearly, while, for the RhB-loading P25, no obvious peaks from RhB are observable (curve e in Figure 7e). Noting that the quantity of RhB-loading sample and P25 were almost the same, we can deduce that the mass ratio of RhB adsorbed by the $cSiO_2@mSiO_2@TiO_2$ fibers was much higher than that by P25. Figure 7f1−f4 shows the digital images of dried $cSiO_2@mSiO_2@TiO_2$ fibers mat and P25 powders before and after saturated adsorption of RhB. The original $cSiO_2@mSiO_2@TiO_2$ fibers and P25 powders were both white. After saturated adsorption of RhB, the fibers became deep purple red, while the P25 powders presented a light orange color. The above results demonstrate that the RhB in water can be more effectively pre-gathered around the TNWs on the fibers before photocatalytic degradation.

Photocatalysts are usually used in terms of suspensions or films, wherein films are superior over suspensions due to their small footprints, which can significantly reduce the capital costs of infrastructure.[39] The high flexibility made the $cSiO_2@mSiO_2@TiO_2$ fibers easy to be processed into nonwoven film. In this investigation, we evaluated the ability of such film for removal of organic pollutant from water merely through filtration accompanied by UV irradiation. Detail for preparation of the film and the water purification procedure can be found in the Experimental Section. As shown by the left image in Figure 8a, 0.12 g of $cSiO_2@mSiO_2@TiO_2$ fibers were patterned into a disk-shaped film with a diameter and thickness of 3.2 cm and 0.7 mm, respectively. High flexibility of the film was readily retained; the $cSiO_2@mSiO_2@TiO_2$ film could be curled and remained integral without any breakage (the right image in Figure 8a). The 20 mL aqueous solution containing 120 μg of RhB faded remarkably, after passing through the film with a flow rate of 60 mL·h^{-1} (Figure 8b, the red line). Quantitative measurement revealed that the concentration of RhB decreased from 6 to 2.4 mg·L^{-1}; roughly 60% RhB was conveniently removed with the film. The absorption peak centering at about 553 nm, which originated from the vibration of ethyl groups of the RhB molecules (see Figure S3, Supporting Information), shifted to shorter wavelength along with the increase of the filtration cycles and almost disappeared after eight cycles of filtration (as demonstrated by the purple line in Figure 8b), indicating that the RhB was almost completely de-ethylated. The removal efficiency of RhB through filtration with the film increased with the decrease of the initial concentration of RhB. Figure 8c shows the visible absorption spectra of RhB solution with various concentrations before and after filtration (accompanied by UV irradiation). When the initial RhB concentration varied from 240 to 24 mg·L^{-1} and then to 6 mg·L^{-1}, the removal efficiency of RhB increased from 36 to 49%, and then to 64%. While the initial concentration of RhB decreased to 2.4 mg·L^{-1}, higher than 95% removal efficiency was achieved only via one cycle of filtration. This indicates that the $cSiO_2@mSiO_2@TiO_2$ film is especially useful for purification of polluted water with very low concentration of organic pollutants with relatively high flux. The film thickness was also investigated as a factor that influenced the water purification efficiency of the $cSiO_2@mSiO_2@TiO_2$ film. Three bottles of 20 mL RhB aqueous solutions with a concentration of 6 mg/L were separately filtrated by three pieces of $cSiO_2@mSiO_2@TiO_2$ films under UV irradiation. As presented in Figure 8d, the intensity of the characteristic absorption peaks of the RhB solution descended remarkably after filtration. Intensity decrease of the absorption peaks of RhB increased with the increase of the film thickness. The RhB removal efficiency of the films with thicknesses of 0.4, 0.7, and 1 mm was calculated to be 54, 77, and 88%, respectively.

In practical application, for example, remediation of natural water (lake water, river water, etc.), repeated use of the film will inevitably lead to accumulation of pollutants (for example, water bloom) and degrade the photocatalysis efficiency of the

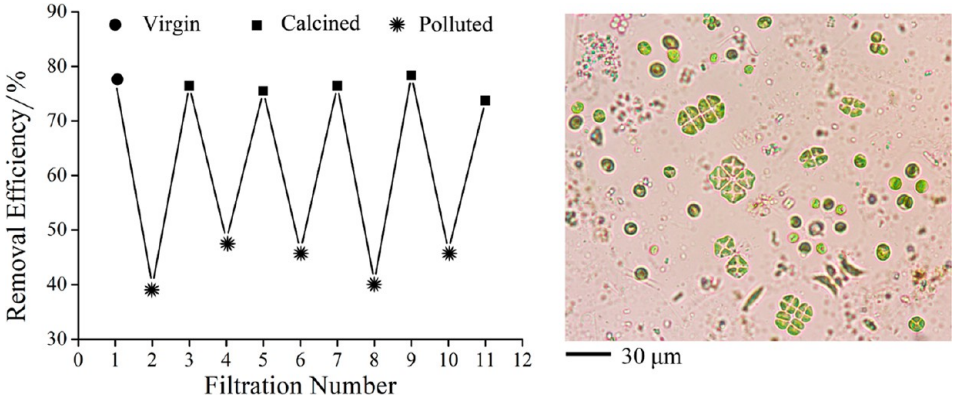

Figure 9. Regeneration ability of the $cSiO_2@mSiO_2@TiO_2$ film (thickness: 0.7 mm). The left graphic shows the removal efficiency of virgin film (as-made sample, the black disk), polluted film (deposited with water bloom, black star), and regenerated film (calcined at 580 °C for 3 h, black cubic). The right picture shows the microscopy image of the water blooms used in this investigation.

film. Previous investigations on flexible freestanding films made from micro- and nanofibers for water purification mainly focused on polymer as fiber matrix. The poor thermal resistance of polymer makes it difficult to bear calcination for elimination of the organic pollutants accumulating on the film and restoring the photocatalytic reactivity. The $cSiO_2@mSiO_2@TiO_2$ film in the present investigation is of completely inorganic nature, which makes it possible to bear high-temperature calcination; consequently, this kind of film possesses high remediation ability. As presented in Figure 9, initially the $cSiO_2@mSiO_2@TiO_2$ film could purify the RhB solution through filtration and UV irradiation with a removal efficiency as high as 77%. After being contaminated by water bloom, the RhB removal efficiency decreased to less than 40%. We treated the contaminated film with drying and calcinations, and found its reactivity was recovered quite well, the removal efficiency restored to higher than 76%, as marked by the first black cubic (from left to right) in Figure 9. Bearing five cycles of the contamination−calcination process, the film still exhibited a RhB removal efficiency of about 74%. This demonstrates that the completely inorganic $cSiO_2@mSiO_2@TiO_2$ film possesses excellent regeneration ability, which can be realized simply via calcination.

4. CONCLUSION

In summary, we have demonstrated a novel and effective approach for constructing TiO_2 based photocatalyst with high reactivity and ease of manipulation in environmental remediation. Continuously long and flexible SiO_2 nanofibers were fabricated utilizing the sol-gel and electrospinning techniques and then cladded with a mesoporous SiO_2 layer, forming a core−shell porous structure. Finally, an additional porous shell of anatase TiO_2 nanowhiskers was muffled over the SiO_2 fiber, constructing a core@double-shell porous architecture, making the fiber appear like a luffa sponge, which we nominated as $cSiO_2@mSiO_2@TiO_2$. Quite different from the electrospinning-derived TiO_2 nanofibers, which suffered from poor mechanical strength, and electrospun polymer nanofibers decorated with TiO_2 nanocrystals, which lacked enough thermal stability, $cSiO_2@mSiO_2@TiO_2$ fibers here simultaneously possess high reactivity, good flexibility, and excellent thermal stability. With rhodamine B as a model water pollutant, the glass−TiO_2 composite fiber demonstrated higher reactivity than the commercial Degussa P25. Reclaiming of the fibers after the photocatalytic reaction can be accomplished very conveniently via simple filtration. The flexible fibers also can be processed into nonwoven film with hierarchical porosity to simplify the environmental remediation procedure. Due to the high thermal stability, the film composed of $cSiO_2@mSiO_2@TiO_2$ fibers possesses excellent regeneration ability from organic pollution, which will offer more convenience in its practical application. Such highly reactive, flexible, and thermally stable glass−TiO_2 composite fiber may find extensive use in environment remediation applications.

■ ASSOCIATED CONTENT

Supporting Information

Figures showing a luminescent spectrum of the UV light source used in this investigation, a schematic illustration of the home-made setup for investigation of the environment purification ability of the $cSiO_2@mSiO_2@TiO_2$ membrane, the molecular structure of rhodamine B, and N_2 adsorption−desorption isotherms and SEM image of Degussa P25 TiO_2 nanopowder. This material is available free of charge via the Internet at http://pubs.acs.org.

■ AUTHOR INFORMATION

Corresponding Author

*E-mail: qjr@scut.edu.cn.

Notes

The authors declare no competing financial interest.

■ ACKNOWLEDGMENTS

This work was financially supported by the National Natural Science Foundation of China (Grant Nos. 51072054, 51072060, 51132004, 51102096), Fundamental Research Funds for the Central Universities (Grant No. 2012ZB0003), Research Funds for Postal Doctoral Students in China (Grant No. 2012M511555), Guangdong Natural Science Foundation (Grant Nos. S2011030001349, 1045106410104887), Guangdong Natural Science Foundation for Distinguished Young Schloars (Grant No. S20120011380), Fok Ying Tong Education Foundation (Grant No. 132004), Chinese Program for New Century Excellent Talents in University (Grant No. NCET-110158), and National Basic Research Program of China (2011CB808100).

REFERENCES

(1) Fujishima, A.; Rao, T. N.; Tryk, D. A. *J. Photochem. Photobiol., C* **2000**, *1*, 1−21.
(2) Wold, A. *Chem. Mater.* **1993**, *5*, 280−283.
(3) Linsebigler, L.; Lu, G.; Yates, J. T. *Chem. Rev.* **1995**, *95*, 735−758.
(4) Tada, H.; Kiyonaga, T.; Naya, S. *Chem. Soc. Rev.* **2009**, *38*, 1849−1858.
(5) Woan, K.; Pyrgiotakis, G.; Sigmund, W. *Adv. Mater.* **2009**, *21*, 2233−2239.
(6) Kumar, S. G.; Devi, L. G. *J. Phys. Chem. A* **2011**, *115*, 13211−13241.
(7) Zhang, Z.; Wang, C.; Zakaria, R.; Ying, J. Y. *J. Phys. Chem. B* **1998**, *102*, 10871−10878.
(8) Shchukin, D. G.; Schattka, J. H.; Antonietti, M.; Caruso, R. A. *J. Phys. Chem. B* **2003**, *107*, 952−957.
(9) Cesano, F.; Pellerej, D.; Scarano, D.; Ricchiardi, G.; Zecchina, A. *J. Photochem. Photobiol., A* **2012**, *242*, 51−58.
(10) Zhu, J.; Wang, J.; Lv, F.; Xiao, S.; Nuckolls, C.; Li, H. *J. Am. Chem. Soc.* **2013**, *135*, 4719−4721.
(11) Kim, C.; Shin, J.; Cho, Y.; Jang, H.; Byun, H.; Kim, T. *Appl. Catal. A* **2013**, *455*, 211−218.
(12) Lu, J.; Zhang, P.; Li, A.; Su, F.; Wang, T.; Liu, Y.; Gong, J. *Chem. Commun.* **2013**, *49*, 5817−5819.
(13) Jiang, Z.; Kong, Liang.; Alenazey, F. S.; Qian, Y.; France, L.; Xiao, T.; Edwards, P. P. *Nanoscale* **2013**, *5*, 5396−5402.
(14) Li, D.; Xia, Y. *Nano Lett.* **2003**, *3*, 555−560.
(15) Liu, Z.; Sun, D. D.; Guo, P.; Leckie, J. O. *Nano Lett.* **2007**, *7*, 1081−1085.
(16) Doh, S. J.; Kim, C.; Lee, S. G.; Lee, S. J.; Kim, H. *J. Hazard. Mater.* **2008**, *154*, 118−127.
(17) Kim, J.; Shi, D.; Kong, K.; Heo, Y.; Kim, J.; Jo, M.; Lee, Y.; Kang, Y.; Dou, S. *ACS Appl. Mater. Interfaces* **2013**, *5*, 691−696.
(18) Zhao, T.; Liu, Z.; Nakata, K.; Nishimoto, S.; Murakami, T.; Zhao, Y.; Jiang, L.; Fujishima, A. *J. Mater. Chem.* **2010**, *20*, 5095−5099.
(19) Im, J. S.; Kim, M. I.; Lee, Y. S. *Mater. Lett.* **2008**, *62*, 3652−3655.
(20) Bazarjani, M. S.; Hojamberdiev, M.; Morita, K.; Zhu, G.; Cherkashinin, G.; Fasel, C.; Herrmann, T.; Breitzke, H.; Gurlo, A.; Riedel, R. *J. Am. Chem. Soc.* **2013**, *135*, 4467−4475.
(21) Peter, A.; Mihaly-Cozmuta, L.; Mihaly-Cozmuta, A.; Nicula, C. *Int. J. Appl. Ceram. Technol.* **2013**, 1−14.
(22) Takeuchi, M.; Hidaka, M.; Anpo, M. *J. Hazard. Mater.* **2012**, *237-238*, 133−139.
(23) Kim, S.; Lim, S. K. *Appl. Catal., B* **2008**, *84*, 16−20.
(24) Yang, M.; Zhang, N.; Xu, Y. *ACS Appl. Mater. Interfaces* **2013**, *5*, 1156−1164.
(25) Inumaru, K.; Kasahara, T.; Yasui, M.; Yamanaka, S. *Chem. Commun.* **2005**, 2131−2133.
(26) Pinhoa, L.; Hernández-Garridob, J. C.; Calvinob, J. J.; Mosquera, M. J. *Phys. Chem. Chem. Phys.* **2013**, *15*, 2800−2808.
(27) Uddin, M. J.; Cesano, F.; Bonino, F.; Bordiga, S.; Spoto, G.; Scarano, D.; Zecchina, A. *J. Photochem. Photobiol., A* **2007**, *189*, 286−294.
(28) Uddin, M. J.; Cesano, F.; Scarano, D.; Bonino, F.; Agostini, G.; Spoto, G.; Bordiga, S.; Zecchina, A. *J. Photochem. Photobiol., A* **2008**, *199*, 64−72.
(29) Uddin, M. J.; Cesano, F.; Bertarione, S.; Bonino, F.; Bordiga, S.; Scarano, D.; Zecchina, A. *J. Photochem. Photobiol., A* **2008**, *196*, 165−173.
(30) Lee, J. A.; Krogman, K. C.; Ma, M.; Hill, R. M.; Hammond, P. T.; Rutledge, G. C. *Adv. Mater.* **2009**, *21*, 1252−1256.
(31) Horzum, Nesrin.; Muñoz-Espí, R.; Glasser, G.; Demir, M. M.; Landfester, K.; Crespy, D. *ACS Appl. Mater. Interfaces* **2012**, *4*, 6338−6345.
(32) Iguchi, Y.; Ichiura, H.; Kitaoka, T.; Tanaka, H. *Chemosphere* **2003**, *53*, 1193−1199.
(33) Peng, X.; Santulli, A. C.; Sutterb, E.; Wong, S. S. *Chem. Sci* **2012**, *3*, 1262−1272.
(34) Ma, Z.; Ji, H.; Teng, Y.; Dong, G.; Zhou, J.; Tan, D.; Qiu, J. *J. Colloid Interface Sci.* **2011**, *358*, 547−553.
(35) Xiong, C.; Balkus, K. J. *Chem. Mater.* **2005**, *17*, 5136−5140.
(36) Xiong, C.; Kim, M. J.; Balkus, K. J. *Small* **2006**, *2*, 52−55.
(37) Xiong, C.; Balkus., K. J. *J. Phys. Chem. C* **2007**, *111*, 10359−10367.
(38) Yang, D.; Paul, B.; Xu, W.; Yuan, Y.; Liu, E.; Ke, X.; Wellard, R.M.; Guo, C.; Xu, Y.; Sun, Y.; Zhu, H. *Water Res.* **2010**, *44*, 741−750.
(39) Bai, H.; Liu, Z.; Sun, D. D. *Chem. Commun.* **2010**, *46*, 6542−6544.